Jurnal
Teknologi

Full Paper

ENVIRONMENTAL INFLUENCE MONITORING ON A HYBRID PHOTOVOLTAIC-THERMOELECTRIC GENERATION UTILIZING THE INTERNET OF THINGS

Waluyo*, Arsyad Ramadhan Darlis, Febrian Hadiatna, Ahmad Abimanyu, Ginulur Farhandika Maulana

Department of Electrical Engineering, Institut Teknologi Nasional Bandung, Jalan KHP Hasan Mustopa No. 23, Bandung, 40124, West Java, Indonesia

Article history
Received
24 May 2025
Received in revised form
25 October 2025
Accepted
2 November 2025
Published Online
29 August 2026

*Corresponding author
waluyo@itenas.ac.id

Graphical abstract

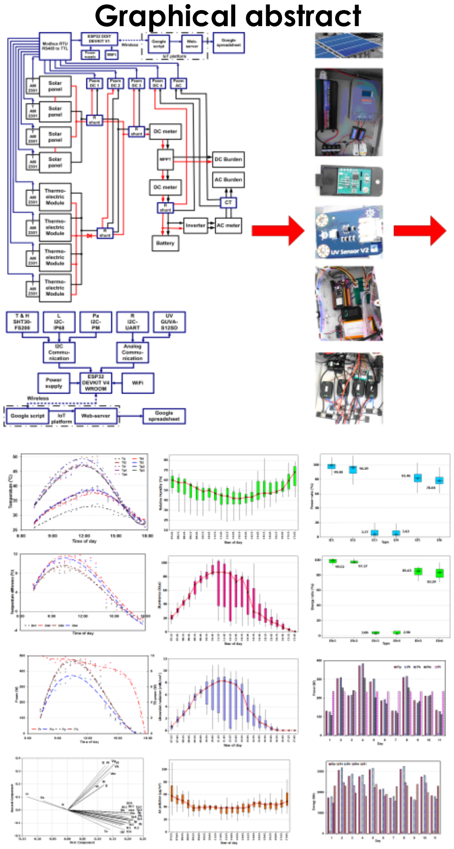

Abstract

Renewable energy, such as a hybrid photovoltaic-thermoelectric (PVTE) power generation, reduces dependence on conventional energy sources and gas emissions. This generation is installed outdoors, so various environmental factors continuously and simultaneously influence its performance. Therefore, these continuous and simultaneous effects on PVTE power generation should be accurately investigated through data acquisition employing the Internet of Things (IoT) and corresponding sensors. The electrical parameters employed PZEM-016 and PZEM-017 sensors, whereas the environmental parameters employed SHT30-FS200, I2C-IP68, Guva-S12SD, I2C air quality PM, and I2C-UART tipping bucket sensors for temperature and humidity, illuminance, ultraviolet (UV) radiation, pollution, and rainfall sensing, respectively. Meanwhile, AM2301 devices sensed photovoltaic (PV) and thermoelectric (TE) module temperatures. Principal component analysis (PCA), box plot, and correlation coefficient were employed for data analysis. The two highest environmental parameters that influence the PV, hybrid, and MPPT (Maximum Power Point Tracking) powers were UV radiation and illuminance, with a high correlation range between 0.820 and 0.863. While the TE power was moderately influenced by the temperature difference, with a correlation coefficient range of 0.511 - 0.542. The power-increasing rates due to illuminance were 2.61 watts/klux and 0.01 watts/klux for the PV and TE modules, respectively. The power ratios were 99.40% and 78.04%, and the energy ratios were 99.52% and 83.29% for the hybrid point and MPPT, respectively.

Keywords: Correlation, environmental factor, photovoltaic, ratio, thermoelectric

1.0 INTRODUCTION

Climate change, one of the sources of which is CO_2 gas, has critically caused global warming. Therefore, decarbonization is mandatory through the development of electric generation based on renewable energy sources, such as photovoltaic, thermoelectric, and wind [1]. This energy should be converted to electrical parameters and associated equipment, such as alternating current (AC) to or from direct current (DC) conversions [2]. Solar energy is converted to electricity by PV (photovoltaic) and TE (thermoelectric) modules, utilizing sunlight and heat, respectively [3], as well as power and efficiency generation experienced enhancements [4-5]. Technically, this case utilizes phase change materials and solar collectors [6], combining PV radiated and TE cooling (PVRC-TEC) [7], adding passive cooling [8], and a high-quality passivation layer [9].

Actually, PVTE (photovoltaic-thermoelectric) generators are installed outdoors, where many environmental factors simultaneously and continuously influence their performance. These factors always change daily, and even change from day to day. Consequently, the PVTEs' performance, indicated by the yielded power, also changes. Research on the PVTEs' performance due to environmental influences is limited, as well as the involvement of environmental parameters. The correlations have been investigated between power and temperature [6, 10-11] and power versus solar radiation [6, 12-13], air pollution [12-14], air pollution and soiling effects [15-16], and rainfall [17-19], as well as rainfall and snow [20-21]. The remaining environmental parameters, such as humidity, illuminance, and UV radiation, should also be elaborated.

Furthermore, the power flow should be monitored and analyzed in more detail in some sections of the generating system. Because the environmental parameters influence the PVTEs' performance simultaneously and continuously, as closely as possible, the recording data should also be conducted in the same manner. Therefore, this research developed a PVTE power generation system, including more electrical and environmental parameter data recording using the Internet of Things (IoT), to investigate its performance due to the natural environmental variations. The PVTE performance is indicated by voltage, current, power, and energy, as well as power and energy ratios. The environmental parameters were the surrounding air temperature, humidity, illuminance, pollution, rainfall, and UV radiation. Furthermore, the PV and TE module temperatures were also recorded. Moreover, statistical tools, such as PCA (principal component analysis), box plot, and correlation coefficient, should also be employed to analyze the yielded recording data in robust conditions, besides the successfully assembled system. The new contributions are correlations among more environmental parameters and a more comprehensive sorting of sections in the generating system using the statistical tools.

This manuscript consists of four sections. The first section introduces the research background, gaps, objectives, and new contributions. The second section delivers research methods on power and IoT connection design, implementation, computation, and statistical analysis. Moreover, the third section consists of research results and discussion, including environmental and electrical monitoring assembled kits, yielded recording data, processed data of parameter functions, statistically processed data, power and energy daily variations, as well as power and energy ratios. Finally, the fourth section concludes the research results and discussion.

2.0 METHODOLOGY

Figure 1 shows the schematic illustration of the designed hybrid PVTE power system. The power sources comprised four PV modules of 150 Wp and four TE packages. Every two PV modules were connected in series. Both series connections of PV modules were circuited in parallel. The TE package connections were in parallel. Every TE package consisted of 75 modules, whereas every module had a maximum capacity of 3.1 watts, connected in series. To prevent the PV module current flowing into the TE packages, three diodes should be installed in parallel on the TE output, which has a capacity of 6 amperes each.

The combination of the power sources entered an MPPT. Furthermore, the MPPT was connected to a battery and an inverter. A small part of the DC power from the MPPT (Maximum Power Point Tracking) supplied two 12V, 0.3A exhaust fans, as a DC burden of the cooling system. Moreover, the PVTE main power supplied the battery and the inverter. Finally, the power supplied to the AC main burden of LED (light-emitting diode) lamps [22].

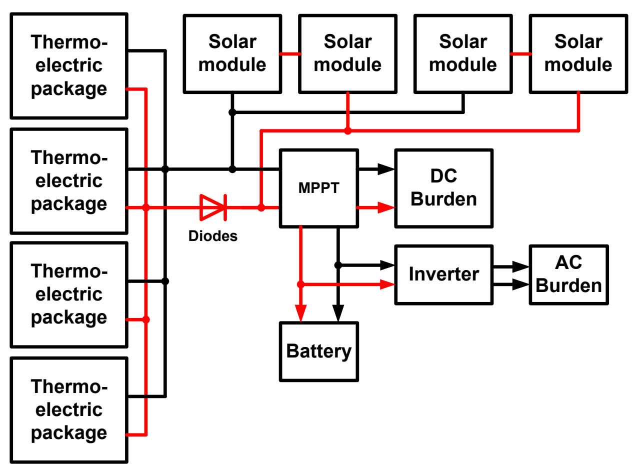

Figure 1 Power flow diagram of PVTE generation

Figure 2 shows the block diagram of the power recording system, including meters, sensors, and the IoT system. Eight AM2301 sensors sensed the PV and TE module temperatures, installed on every module. The DC electrical parameters were sensed on the outputs of the PV modules, TE packages, PV and TE combination, and MPPT output by FL-2.05DC50A shunt resistors. While a PZCT10020 current transformer (CT) sensed the AC electrical parameter at the main burden. Furthermore, Pzem-017s and Pzem-016 converted the DC and AC electrical data, respectively, for entering a Modbus RTU RS-485 to TTL (transistor-transistor logic). Moreover, the data were sent to the first microprocessor of the ESP32 Doit Devkit V1. The first 5V DC power supply was employed to furnish energy to the microprocessor. Moreover, the first modem (modulator-demodulator) was operated and connected to the microprocessor. It provided wireless internet communication through Wi-Fi. Google scripts were employed for hardware integration into the software. It required a web server for web-based data storage. The data were recorded every five minutes. The end data were Google spreadsheet forms, which were read and opened by a laptop or smartphone.

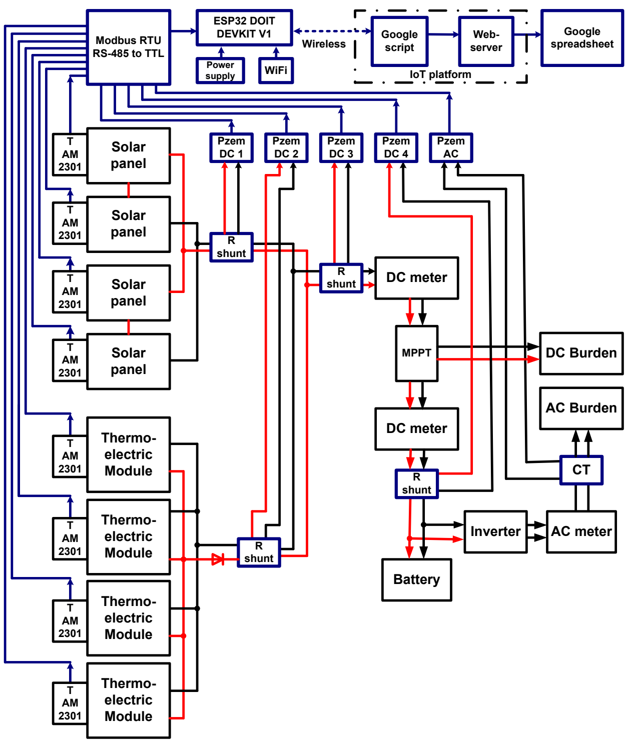

Figure 2 Internet-based power monitoring schematic diagram

Figure 3 shows the internet-based monitoring schematic system diagram of the environmental parameters. These included surrounding air temperature (Ta) and humidity (H), illuminance (L), pollution (Pa), rainfall (R), and UV radiation, which employed SHT30-FS200, I2C-IP68, I2C-PM, I2C-UART, and GUVA-S12SD sensors, respectively.

An Inter-Integrated Circuit (I2C) protocol communication passed the air temperature, humidity, illuminance, and pollution recording data. While an analog communication passed the rainfall and UV radiation recording data. The data were sent to the second microcontroller of ESP32DevkitV4Wroom. A second 5V DC power supply furnished energy to the second microprocessor. Moreover, a second modem was connected to the second microprocessor. It served the internet wireless communication through Wi-Fi. Finally, the treatment was the same as that of the electrical parameter monitoring system.

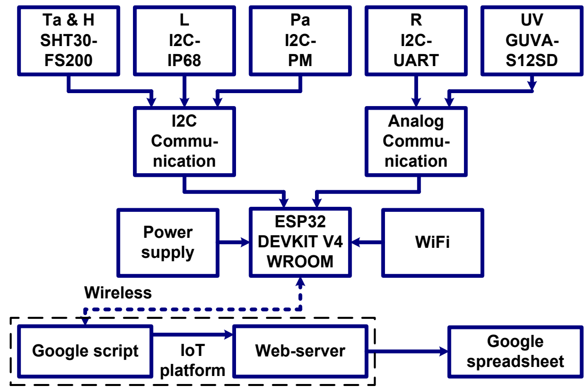

Figure 3 Internet-based environmental monitoring schematic diagram

Furthermore, the energies were computed by numerical integration of composite Simpson's 1/3 rule [23], as in equation (1).

$$I = \frac{1}{3}h\left(f_0 + 4\sum_{i=1}^{n} f_{2i-1} + 2\sum_{i=1}^{n-1} f_{2i} + f_n\right) \quad (1)$$

Meanwhile, the computations of typical (median) output-input power and energy ratios follow equations (2) and (3), respectively.

$$r_p = \frac{P_o}{P_i} x100\% \quad (2)$$

$$r_e = \frac{E_o}{E_i} x100\% \quad (3)$$

where r_p, r_e, P_i, P_o, E_i, and E_o are power ratio, energy ratio, input power, output power, and input energy, as well as output energy, respectively. Furthermore, the yielded data were analyzed using the correlation coefficient, boxplot [24-26], and PCA [27-28]. The correlation coefficient essentially follows equation (4).

$$r = \frac{s_{xy}}{s_x . s_y} \quad (4)$$

where r, x, y, s_x, s_y, and s_{xy} are the correlation coefficient, independent variables, dependent variables, standard deviations of x, standard deviations of y, and covariance between x and y, respectively.

PCA was used to reduce groups of variables into subsets represented by latent constructs. Generally, PCA computations have some steps, such as standardization, covariance matrix, eigenvector and eigenvalue computations, vector featuring, and data recasting along PCA axes. The PCA specifies variable factors in decreasing importance order. The two-dimensional plot (biplot) contribution degree of information is revealed in equation (5), where β(2) is the contribution rate [24], and λ_i are eigenvalues [29-31].

$$\beta(2)=\frac{\lambda_1+\lambda_2}{\sum_{i=1}^{n}\lambda_i} \quad (5)$$

The data analyses also used the boxplot (box-and-whisker plot) method [24-26], emphasizing dataset dispersion in the interquartile range and median visual representations [27-28].

3.0 RESULTS AND DISCUSSION

Figure 4 shows several leading equipment for the yielded hybrid PVTE power generation.

(a)

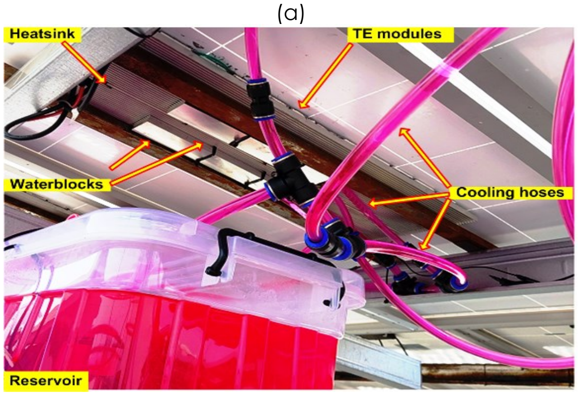

(b)

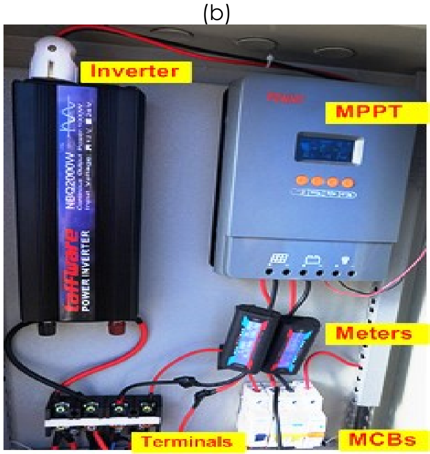

(c)

Figure 4 The leading equipment of the hybrid power system: (a) PV modules, (b) equipment of PV bottom parts, and (c) inverter, MPPT, and meters

Figure 4(a) shows four 150 Wp PV modules, electrically connected in series and parallel. Figure 4(b) shows the bottom parts of PV modules comprised of TE modules, heat sinks, water blocks, cooling hoses, and a reservoir. Furthermore, Figure 4(c) shows the 1000-watt inverter, 12-volt MPPT, some meters, miniature circuit breakers (MCBs), and terminals, connected to a 100 Ah Lithium Iron Phosphate battery. This power installation improved the previous one [22] and includes additional internet-based monitoring systems.

Figure 5 shows the two main supporting apparatuses of internet-based monitoring and data recording. Figure 5(a) shows the sensor to measure PV and TE module temperatures. Meanwhile, Figure 5(b) shows the UV radiation sensor of the environmental parameter.

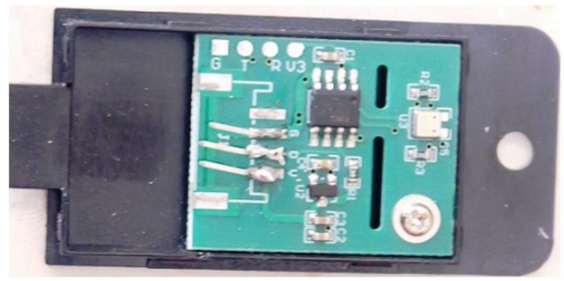

(a)

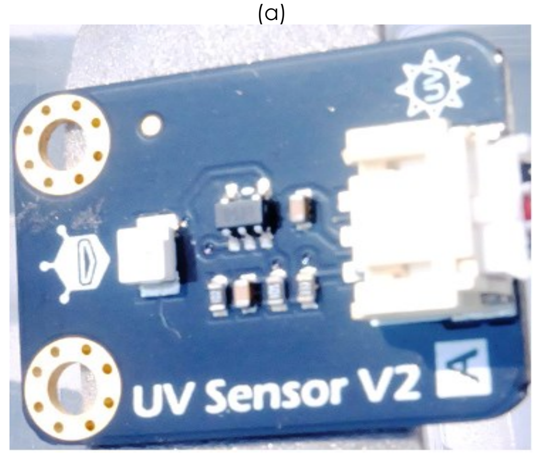

(b)

Figure 5 Sensing devices for IoT-based data recording: (a) temperature and (b) UV sensors

Figure 6(a) is the environmental monitoring kit, connected to the environmental parameter sensors. The notations are connector pins, ESP32 board, voltmeter display, DC-DC converter, and battery for one to five numbers, respectively. Furthermore, Figure 6(b) is the electrical monitoring kit, connected to the electrical parameter sensors. One to seven numbers notate an adapter, modem, ESP32Devkit microprocessor board, Pzem016, four Pzem017s, 100 A shunt resistors, and wiring terminals, respectively. Both kits also made connections to the microcontroller-based data-logging circuits.

(a)

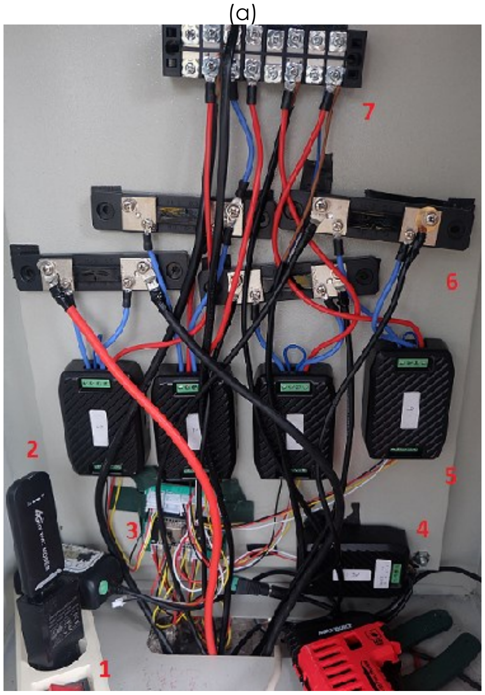

(b)

Figure 6 IoT-based data recording: (a) environmental and (b) electrical monitoring kits

Figure 7 shows a sample of the yielded recording data of the surrounding air temperature and humidity. Typically, in the morning, the air temperature increases and reaches midday, around 12:00. After that, it decreased until the evenings. The opposite condition was for the ambient humidity. In the morning, the ambient humidity decreased and reached its bottom, around 12:00 o'clock. After that, the ambient humidity increased until the evenings. The behaviors that were similar to temperature were first to fourth PV module temperatures, first to fourth TE package temperatures, PV power, TE power, hybrid power, and MPPT powers, illuminance, and UV radiation. While the air pollution increased and reached its peak in the morning. Finally, rainfall is infrequent. If it does rain, it's usually between 3 and 5 p.m.

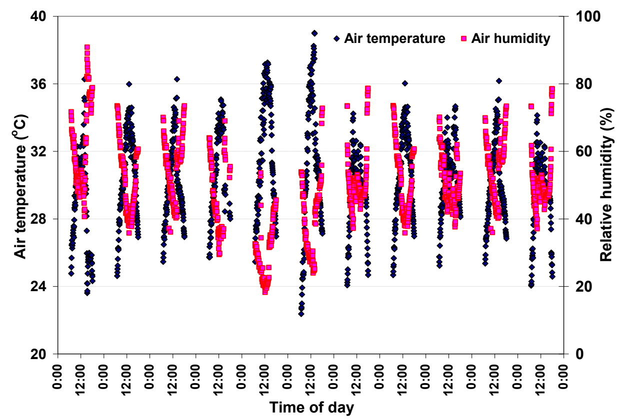

Figure 7 Surrounding air temperature and humidity recording data

Table 1 Recording data recapitulation

Parameter (unit)	Sensed medium	Maximum median	Median
Temp. (°C)	PV 1	52.5	39.2
Temp. (°C)	TE 1	42.7	33.8
Temp. (°C)	PV 2	55.3	40.7
Temp. (°C)	TE 2	42.2	34.0
Temp. (°C)	PV 3	52.6	39.0
Temp. (°C)	TE 3	41.5	34.0
Temp. (°C)	PV 4	52.6	39.3
Temp. (°C)	TE 4	40.9	33.3
Power (W)	PVs	494.3	203.5
Power (W)	Hybrid	509.1	202.1
Power (W)	TEs	11.0	8.6
Power (W)	MPPT	435.2	182.8
Temp. (°C)	Air	36.0	30.3
RH (%)	Air	36.0	48.6
Illuminance (klux)	Air	99.4	36.7
UV (mW/cm²)	Air	9.4	2.4
Pollution (µg/m³)	Air	74.0	41.0

The testing samples were carried out for eleven days. Table 1 lists the recapitulation of recording data based on the median of maximum values and median values. The range of the typical peak PV and TE temperature differences was 9.8°C-13.1°C, with 11.4°C median and mean values. While the range of the typical temperature differences was 5.0°C-6.8°C, with 5.7°C and 5.8°C, median and mean values, respectively.

Meanwhile, the minimum and maximum recording data on the air surrounding temperature, humidity, illuminance, UV radiation, pollution and rainfall were 15.0°C and 39.0°C, 18.2% and 90.8%, 0 klux and 105.7 klux, 0 mW/cm² and 11.0 mW/cm², 6 μg/m³ and 125.0 μg/m³, and 0 mm and 29.4 mm, respectively. Based on the yielded recording data, the sensors and internet-based monitoring system operated appropriately. Therefore, the data could be further analyzed.

Trends of the typical (median) parameter recording data were made using time-of-day functions. Figure 8(a) shows the typical surrounding air temperature (Ta), the first up to fourth PV module typical temperatures (Tp1, Tp2, Tp3, Tp4), and the first up to fourth TE module typical temperatures (Tt1, Tt2, Tt3, Tt4). Generally, as a function of time of day, the PV module temperatures were the highest, followed by those of the TE modules and the surrounding air temperature, respectively. The typical temperatures reached peak values at around 12:45 until 13:15. There were 48.0°C, 50.2°C, 48.5°C, 48.8°C, 39.9°C, 40.0°C, 39.7°C, 39.1°C, and 33.9°C, for Tp1, Tp2, Tp3, Tp4, Tt1, Tt2, Tt3, Tt4, and Ta, respectively. In the morning, the typical temperature increasing rates every half hour were 0.93°C, 1.10°C, 1.30°C, 0.95°C, 0.83°C, 0.73°C, 0.65°C, 0.90°C, and 0.72°C. While, in the afternoon, the decreasing rates were -1.95°C, -2.70°C, -1.90°C, -2.20°C, -1.25°C, -1.20°C, -1.25°C, -1.50°C and -0.65°C in same time interval for Tp1, Tp2, Tp3, Tp4, Tt1, Tt2, Tt3, Tt4, and Ta, respectively. Compared to the air temperature, at around 07:15, the TE temperatures were 1.05 to 1.06 times, whereas the PV temperatures were 1.27 to 1.28 times. At the middays, from around 11:45 until 12:45, TE temperatures were between 1.13 and 1.18 times, and the PV temperatures were 1.43 and 1.52 times compared to the air temperatures. At around 17:45, the TE temperature to ambient temperature comparisons ranged from 1.01 to 1.03 times, and the PV temperature to ambient temperature comparisons ranged from 0.95 to 0.96 times. Thus, at middays, besides increasing the typical temperatures to be the highest, the TE and PV temperature comparisons to the ambient were also the highest. In the late afternoon, the TE temperatures were slightly higher, and the PV temperatures were somewhat lower than the ambient temperature. The increasing temperatures in the morning, reaching the peaks at midday and decreasing in the afternoon are in line with [32-34], implied in [12, 35-37], PV and TE module temperatures conformed to [11, 38], PV module temperatures conformed to [20, 38-40], implied in [41], and PV and ambient temperatures was implied in [21]. Nevertheless, these research results show that the decreasing rates are considerably higher than the increasing rate magnitudes.

Figure 8(b) shows the typical temperature differences between the corresponding first (Dt1), second (Dt2), third (Dt3), and fourth (Dt4) PV and TE modules. In the morning, these temperature differences increased to midday and decreased to below zero in the evening. The typical growing rates every half-hour were 0.40°C, 0.30°C, 0.30°C, and 0.30°C, for the analogous same-order temperature differences. These typical temperature differences reached the peak values at around 11:45, being 9.25°C, 11.8°C, 9.35°C, and 10.85°C for the first up to fourth corresponding temperature differences, respectively. Furthermore, the decreasing rates of the temperature differences were -0.63°C, -0.90°C, -0.75°C, and -0.68°C in thirty minutes for the same order temperature differences. These values started to be lower than zero between 16:15 and 16:45. These temperature differences were implied in [10, 36] and mentioned in [33], which showed by the TE temperature gap and differences between the PV module rear sides and cooling system temperatures [21].

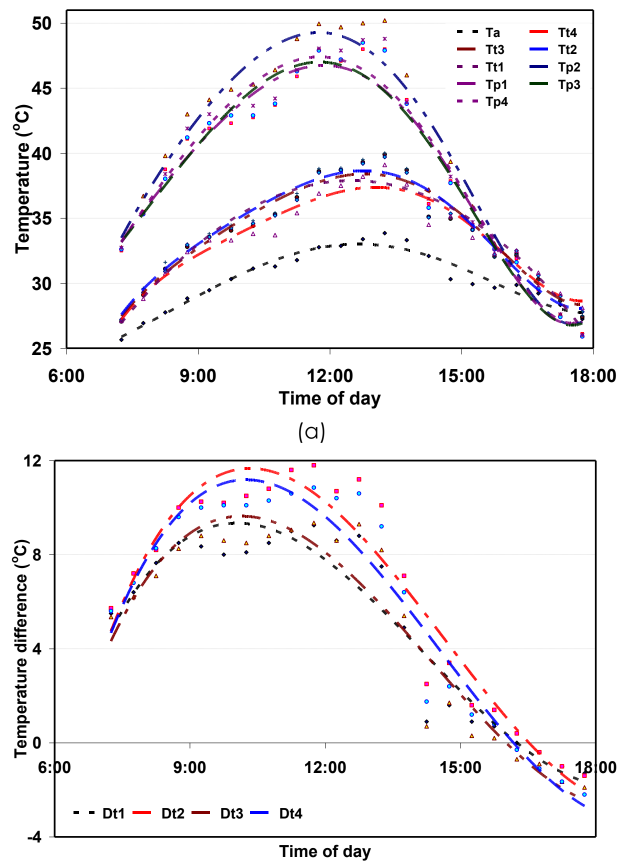

(a)

(b)

Figure 8 Typical (a) temperatures and (b) temperature differences in time of day

Figure 9(a) shows the typical box plots of relative humidity (RH) at various times of day. These values are based on the interquartile range and median values. It typically decreased in the morning to its lowest point at midday and increased in the afternoon. Every thirty minutes, the typical decreasing and rising rates were -2.33% RH and 1.69% RH in the morning and afternoon, respectively. Thus, the drying was faster than the wetting of the air during the day. The minimum values of the RH reached 44.72%, 44.115%, 41.87%, 41.53%, and 42.89% median values, as well as 41.11%, 42.11%, 40.60%, 40.03%, and 40.48% mean values at around 11:45, 12:15, 12:45, 13:15, and 13:45, respectively. This humidity behavior is implied in [32] and conforms to [34, 36].

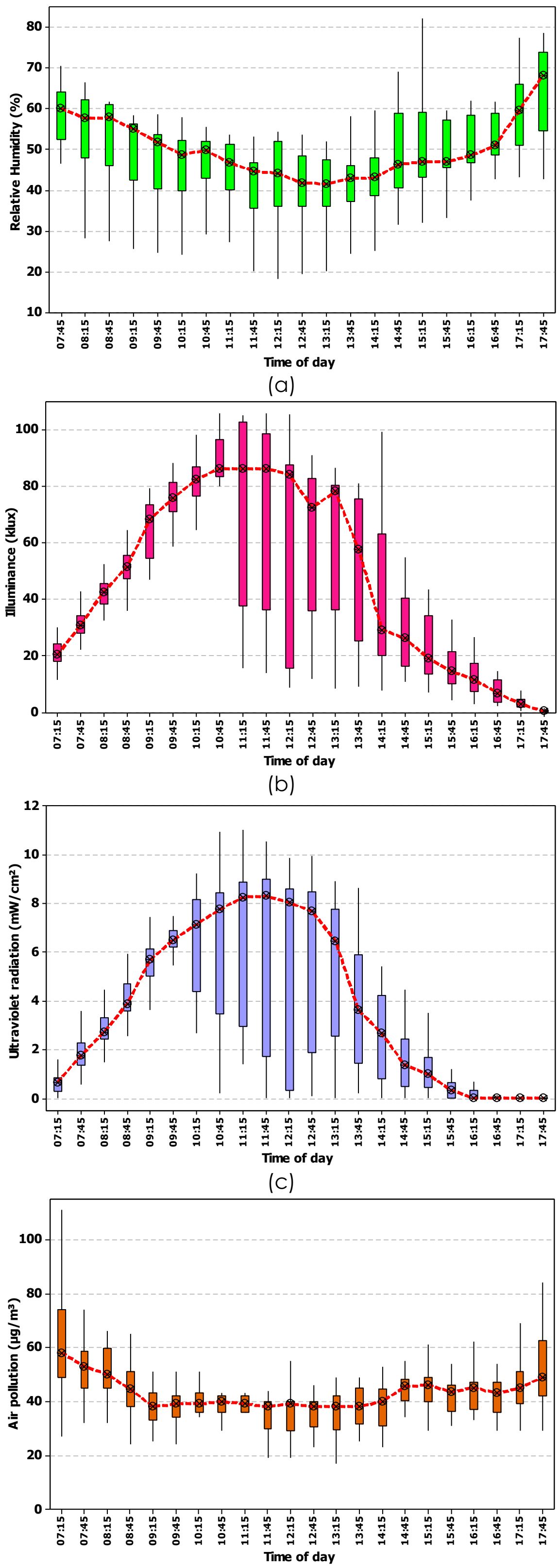

Figure 9 Typical (a) RH, (b) illuminance, (c) UV radiation, and (d) air pollution by time of day

Figure 9(b) shows the box plots of the illuminance at various times of day. No doubt, it reached maximum values at around midday, which were 86:33 klux, 86.36 klux, 86.36 klux, and 84.18 klux median values, and 81.74 klux, 73.39 klux, 72.43 klux, and 61.80 klux mean values, at around 10:45, 11:15, 11:45, and 12:15, respectively. The typical illuminance rising and decreasing rates every half-hour were 8.08 klux and -4.28 klux in the morning and afternoon, respectively. The rising illuminance in the morning, and reached the peaks at midday, and decreasing illuminance in the afternoon were implied in [42], the illuminance in sub-scenario comparisons, in [40] as plane illuminance, in [11, 29, 37, 39] as solar irradiance, in [21] as solar irradiance in time series, implied in [36], and conformed to [43].

Figure 9(c) shows the UV radiation at various times of day in the quartile range and median values. It reached maximum values of 8.24 mW/cm², 8.29 mW/cm², and 8.02 mW/cm² median values, and 6.67 mW/cm², 6.29 mW/cm², and 5.52 mW/cm² mean values at around 11:15, 11:45, and 12:45, respectively. The mean values were considerably lower than the median values due to higher ranges than at other times. In half an hour, the UV radiation increased and decreased to 0.82 klux and -0.66 klux in the morning and afternoon, respectively. The increasing UV radiation in the morning and reaching the peaks was consistent with [44, 45-47], implied in [11, 36-37, 39, 43, 48] as daily solar irradiance.

Figure 9(d) shows the box plots of the typical surrounding air pollution concentration at various times of day. The maximum values were reached in the morning, being 58.00 μg/m³ median and 62.67μg/m³ mean values at around 7:15. The minimum median values were 38.00 μg/m³, 39.00 μg/m³, 38.00 μg/m³, 38.00 μg/m³, and 38.00 μg/m³, whereas the minimum mean values were 36.38 μg/m³, 36.41 μg/m³, 35.98 μg/m³, 35.92 μg/m³, and 38 μg/m³ at around 11:45, 12:15, 12:45, 13:15, and 13:45, respectively. Every half an hour, the typical air pollution decreasing and increasing rates were -1.00 μg/m³ and 1.50 μg/m³ in the morning and afternoon, respectively. The behavior of the slightly reducing air pollution to the bottom point at midday was in line with [15].

All median values of the rainfall were zero. The highest mean value was 1.38 mm, and the highest maximum rainfall was 29.40 mm. Both occurrences were at around 15:45. The maximum rainfall was followed by 8.40 mm and 7.00 mm at around 16:15 and 7:15, respectively. This case indicated that rainfall was very scarce and had considerably low values. The daily rainfall phenomenon, which was relatively high in the morning and afternoon between 15:00 and 16:00, conformed to [18] and was implied in [21].

Figure 10 shows the typical powers at various times of day. These powers were on the PV module (Pp), TE module (Pt), hybrid (Ph), MPPT (Pm), and inverter (Pi). The PV, hybrid, and MPPT powers were relatively low in the morning. They increased and reached a maximum at around midday and went down to around zero values in the evening. Every half an hour, the power increasing and decreasing rates were 47.6 watts and -23.5 watts for the PV modules. While those for the hybrid point were 38.7 watts and -22.4 watts, and 31.0 watts and -22.4 watts for the MPPT output in the morning and afternoon, respectively. The PV-generated power was influenced by the sun's irradiance, so it was low in the morning and evening. It reached the highest value at midday due to the highest irradiance. The PV power dominantly influenced the hybrid and MPPT powers. Meanwhile, the TE-generated power was fairly high in the morning until noon and finally headed to zero in the evening. This case was mainly caused by the high temperature differences in the morning and midday. Moreover, it was caused by the considerably low temperature differences, even negative values, in the evening. The increasing powers to the peaks at middays in line with [32, 43, 49], conformed to [11, 36, 38-39, 41], are implied in [20, 34, 40], and implied and conformed to [35]. Finally, the inverter output power was stable, due to the constant burden, and further decreased in the evening due to limited generated power.

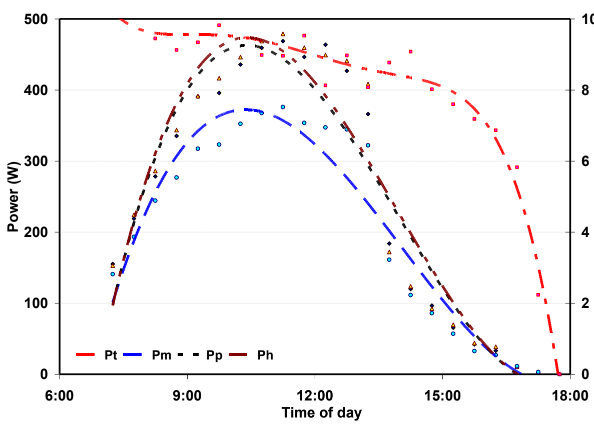

Figure 10 Typical powers at different times of day

Table 2 lists the correlation coefficients among powers: PV modules (Pp), TE modules (Pt), hybrid point (Ph), MPPT output (Pm), and inverter output (Pi) powers in various module temperatures and temperature differences. According to Guilford's informal definition [24], this table shows three categories of correlations: 0.20-0.40 (low), 0.40-0.70 (moderate), and 0.70-0.90 (high). The PV temperature influenced PV, hybrid, and MPPT powers in correlation coefficient ranges of 0.810-0831, 0.796-0.817, and 0.798-0.819, with typical (median) values of 0.824, 0.810, and 0.811, respectively. Therefore, these influences were high categories of correlation coefficient. Although the PVTE temperature differences influenced the three powers in the high category, the PVTE temperature differences were primarily affected by the PV temperatures. Those temperatures and temperature differences influenced these three powers significantly.

Table 2 Correlations among module powers and temperatures

Parameters	Pp	Pt	Ph	Pm	Pi
Tp1	0.810	0.508	0.796	0.798	0.417
Tt1	0.598	0.390	0.590	0.553	0.391
Dt1	0.843	0.511	0.828	0.872	0.338
Tp2	0.829	0.516	0.816	0.815	0.427
Tt2	0.623	0.406	0.615	0.613	0.413
Dt2	0.893	0.539	0.878	0.877	0.373
Tp3	0.818	0.523	0.804	0.806	0.435
Tt3	0.603	0.398	0.595	0.593	0.419
Dt3	0.867	0.542	0.850	0.855	0.363
Tp4	0.831	0.514	0.817	0.819	0.437
Tt4	0.572	0.357	0.564	0.561	0.396
Dt4	0.883	0.542	0.866	0.871	0.387

While the PVTE temperature differences ranged from 0.511 to 0.542, with a median value of 0.541, the correlation coefficient influenced the TE-generated power, being in the moderate category. At the same time, the moderate correlations included the TE temperatures against the PV, hybrid point, and MPPT output powers. Thus, the PV temperature has the highest influence on the PV-generated power, further affecting the hybrid and MPPT output powers.

Table 3 lists the correlation coefficients among powers and environmental parameters. These environmental variables were the surrounding air temperature (Ta), illuminance (L), UV radiation (UV), rainfall (R), pollution (Pa), and humidity (H). The high category of the correlation coefficients included the illuminance and UV radiation against the PV, hybrid, and MPPT output powers. The illuminance affected the PV, hybrid, and MPPT powers, being 0.857, 0.859, and 0.822, respectively. They were high correlation coefficients. While the UV radiation influenced the PV, hybrid, and MPPT powers, with 0.863, 0.863, and 0.820 correlation coefficients, respectively. These were high category. Nevertheless, both environmental parameters influenced the TE and inverter powers in a low category of correlation coefficients between 0.20 and 0.40. Meanwhile, the surrounding air temperature influenced the PV and hybrid powers in the moderate category, slightly larger than 0.40. The humidity decreased the PV and hybrid powers in the moderate category, somewhat less than -0.40. Moreover, the humidity negatively influenced the TE, MPPT, and inverter output powers in the low category with less than -0.40 correlation coefficients. Moreover, the surrounding air temperature slightly influenced the TE power in proportion.

Table 3 Correlations among powers and environmental parameters

Parameters	Pp	Pt	Ph	Pm	Pi
Ta	0.421	0.176	0.416	0.398	0.348
L	0.857	0.392	0.859	0.822	0.404
UV	0.863	0.299	0.863	0.820	0.373
R	-0.084	-0.006	-0.086	-0.086	-0.086
Pa	-0.294	-0.125	-0.303	-0.238	-0.284
H	-0.418	-0.248	-0.412	-0.384	-0.303

Meanwhile, the air pollution negatively influenced the PV, hybrid point, MPPT, and inverter output powers as a low category, with correlation coefficients between -0.20 and -0.40. Furthermore, the air pollution negatively influenced the TE power as a slight category, with a -0.125 correlation coefficient. Finally, the rainfall parameter negatively influenced all powers in a slight category under 0.10 magnitude correlation coefficients. This case conformed to [50]. This meant that the three environmental parameters increased, resulting in a slight decrease in the powers. Among the three parameters, the humidity had the highest correlation to power, with low to moderately negative correlations. The decreasing power due to rising humidity is implied in [21]. The decreasing yield of PV power due to rainfall is implied in [201]. Meanwhile, the power reductions due to increasing air pollution align with [16].

Figure 11 shows the yielded PCA of the electrical system and environmental parameters. The quantities tended to create three groups. The first group consisted of the surrounding air temperature (Ta), UV radiation (UV), illuminance (L), four PV module temperatures (Tp1, Tp2, Tp3, and Tp4), four TE module temperatures (Tt1, Tt2, Tt3, and Tt4), four temperature differences (Dt1, Dt2, Dt3, and Dt4), PV current and power (Ip and Pp), hybrid current and power (Ih and Ph), and MPPT current and power (Im and Pm). Furthermore, the second group consisted of the inverter voltage, current, and power (Vi, Ii, and Pi), TE voltage, current, and power (Vt, It, and Pt), and PV, hybrid, and MPPT voltages (Vt, Vh, and Vm). Finally, the third group consisted of air humidity (H), pollution concentration (Pa), and rainfall (R). The groups indicated that the parameters in every group were directly proportional. The third group is almost exactly the opposite of the first group. Therefore, the surrounding air pollution, humidity, and rainfall caused the electrical parameters in the first group to decrease. Usually, these three environmental parameters decreased as the surrounding air temperature, illuminance, and UV radiation increased. The increasing temperature due to the illumination and UV radiation is implied in [53], which was caused by the solar radiation. Although somewhat far apart, the electrical parameters in the second group are still on the same side as the parameters in the first group, to the right of the center point. Therefore, the electrical parameters in the second group tended to increase slightly when illuminance, air temperature, and UV radiation increased. The retained information was 70.6%, which is representative enough. This case needed to be supported by the box plot or correlation coefficient analyses. The inverse properties of humidity to air temperature, module temperatures, powers, illumination, and UV radiation correspond and are implied in [21]. The power reductions due to increasing air pollution align with [16].

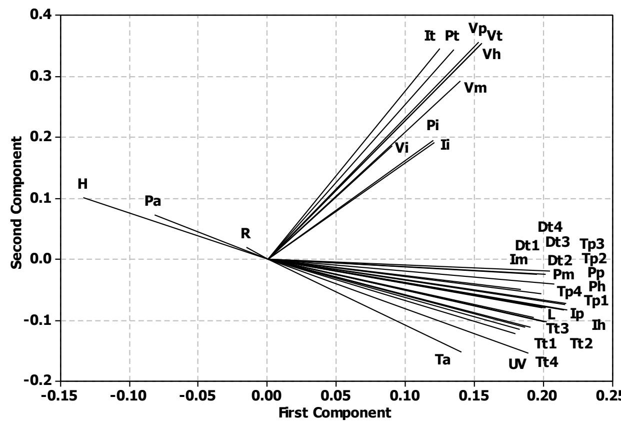

Figure 11 PCA of the parameters

Figure 12(a) shows the typical (median) PV (Pp), TE (Pt), hybrid (Ph), and MPPT (Pm) output powers as a function of the surrounding air temperature. The PV, hybrid, and MPPT output powers increased, reached maximum values, and finally, as the ambient temperature rose. The typical power increasing rates were 25.47 W/°C, 26.87 W/°C, and 24.37 W/°C, whereas the typical power decreasing rates were -76.47 W/°C, -86.55 W/°C, and -57.82 W/°C for the PV, hybrid, and MPPT powers, respectively. They reached the typical maximum values being 310.34 W, 328.88 W, and 260.16 W for the PV, hybrid, and MPPT powers, respectively, in a range between 31.45 °C and 38.24 °C. At the same time, the TE power slightly decreased as the temperature increased, with a mean rate of 0.33 W/°C. This behavior is implied in [5, 10, 32, 34, 37, 43].

Figure 12(b) shows the typical (median) PV (Pp), TE (Pt), hybrid (Ph), and MPPT (Pm) output powers versus the illuminance. Generally, the powers significantly increased as the illuminance rose. At low illuminance, the powers increased drastically; at high illuminance, the powers increased moderately and tended to be saturated. The typical power increasing rates were 2.61 watts/klux, 0.01 watts/klux, 3.33 watts/klux, and 2.72 watts/klux for the PV (Pp), TE (Pt), hybrid (Ph), and MPPT output (Pm) powers, respectively. This typical power dropped drastically at very low illuminance, close to 118.30 watts, or 50.36% of 234.90 watts. This case was caused by the low power-generated illuminance, followed by the low power-generated battery. The increasing power due to illuminance is implied in [4, 21, 51] due to solar radiation. Meanwhile, the typical inverter output was basically constant.

Figure 12(c) shows the typical powers versus UV radiation. The PV (Pp), hybrid (Ph), and MPPT output (Pm) powers significantly increased as the UV radiation rose. The typical (median) power increasing rates were 24.21 watts/(mW/cm²), 27.99 watts/(mW/cm²), and 13.14 watts/(mW/cm²) for the PV (Pp), hybrid (Ph), and MPPT output (Pm) powers, respectively. Meanwhile, TE power (Pt) increased drastically at low UV radiation, and it was further constant and decreased slightly as the UV radiation further increased, with a typical power increasing rate of 0.029 watts/(mW/cm²). It could be said to be fairly constant. The increasing powers due to rising UV radiation are implied in [4, 21, 51], as yielded by solar irradiation. The inverter output power tended to be constant. It experienced a slight drop in low UV radiation due to low generated power illuminance, which means the UV radiation is proportional to the illuminance.

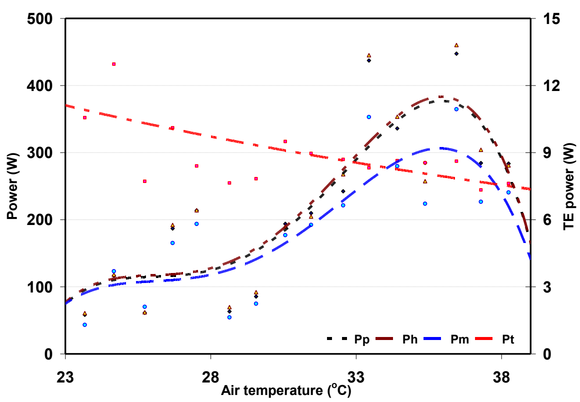

(a)

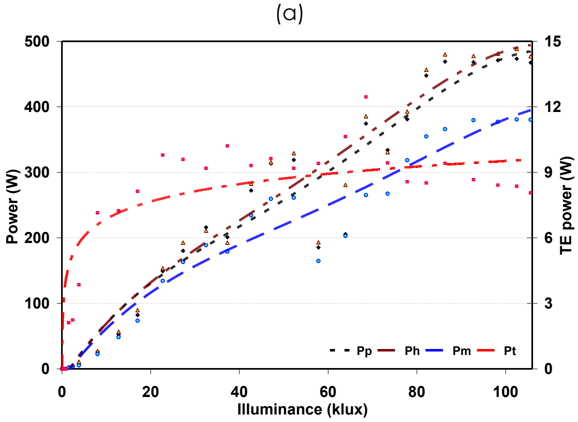

(b)

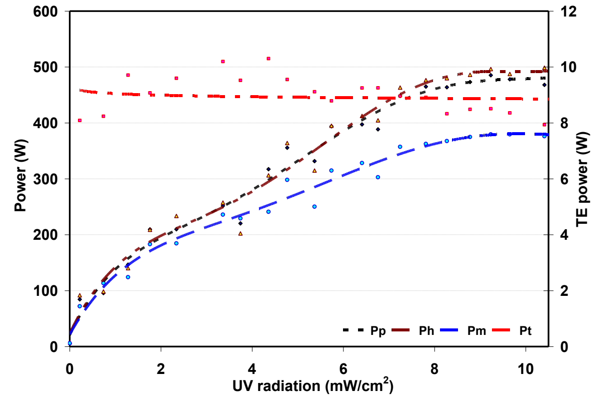

(c)

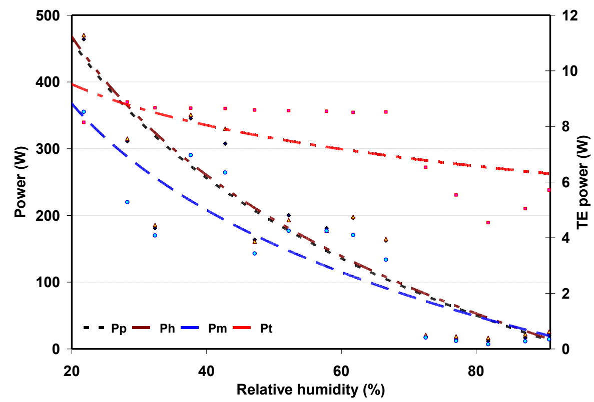

(d)

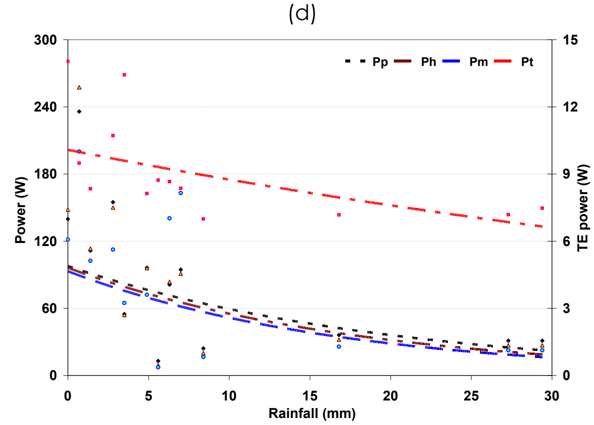

(e)

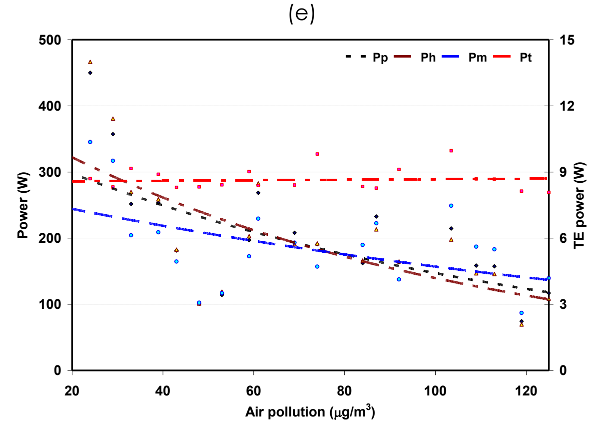

(f)

Figure 12 Typical powers versus (a) air temperature, (b) illuminance, (c) UV radiation, (d) humidity, (e) rainfall, and (f) pollution

Figure 12(d) reveals the typical powers in conformity with the surrounding air humidity. The PV (Pp), hybrid (Ph), and MPPT output (Pm) powers decreased significantly as the air humidity rose. The typical decreasing rates were -3.49 watts/% RH, -3.33 watts/% RH, and -1.33 watts/% RH for the PV, hybrid, and MPPT output powers, respectively. Meanwhile, the TE power decreased slightly as the air humidity increased, with a typical decreasing rate of -0.00456 watts/% RH. This case indicated that the air humidity did not practically influence the TE power. The decreasing power due to rising humidity is implied in [21]. The increasing power due to rising irradiance was followed by a reduction in humidity in the time series. Finally, the inverter output was in a constant condition due to a constant burden, practically unaffected by the air humidity.

Figure 12(e) shows the PV, hybrid, MPPT, and TE output powers versus the rainfall. The first three output powers considerably decreased as the rainfall increased. The exponential decreasing rates were -0.0499 W/mm, -0.0556 W/mm, and -0.0591 W/mm, for the PV, hybrid, and MPPT powers, respectively. Meanwhile, the TE power slightly decreased, with an exponential constant of -0.0141 W/mm. These phenomena are implied in [17, 21].

Figure 12(f) shows the typical powers as functions of the surrounding air pollution. The PV (Pp), hybrid (Ph), and MPPT output (Pm) powers decreased considerably, being -3.44 watts/(μg/m³), -2.19 watts/(μg/m³), and -5.66 watts/(μg/m³), respectively. Furthermore, the TE and inverter output powers tended to be constant. The former proved that the TE modules were practically not influenced by air pollution. The system burden dominantly caused the latter. The power reductions due to increasing air pollution align with [16].

Figure 13(a) shows the typical powers versus PV temperature. The PV (Pp), hybrid (Ph), and MPPT output (Pm) powers increased significantly to maximum values and then decreased drastically. The power increasing rates were 12.94 watts/°C, 7.96 watts/°C, and 9.44 watts/°C for the PV, hybrid, and MPPT output powers, respectively. The typical culminated powers were 467.3 watts, 480.4 watts, and 370.7 watts at a typical PV temperature of 51.3°C for the same order. Meanwhile, the power decreasing rates were -50.70 watts/°C, -54.95 watts/°C, and -40.79 watts/°C, for the same order. It shows that the decreasing rate magnitudes were significantly higher than the increasing rate magnitudes. Furthermore, the typical TE power increasing rate was 0.134 watts/°C, which considerably increased at low PV temperatures and tended to be saturated at high PV temperatures. The decreasing powers at high temperatures align with [3] and are implied in [37-38, 52-54]. Finally, the inverter output power tended to be constant at 234.5 watts. It dropped to 118.3 watts at low PV temperatures due to insufficient generated power.

Figure 13(b) shows the typical (median) powers as a function of PV and TE module temperature differences. The PV (Pp), hybrid point (Ph), and MPPT output (Pm) powers considerably increased as the temperature difference rose and tended to be saturated. The typical power increasing rates were 26.94 watts/°C, 34.20 watts/°C, and 20.07 watts/°C for the PV, hybrid point, and MPPT output powers, respectively. These three powers reached optimum values of 468.6 watts, 485.1 watts, and 373.5 watts at around 10.5°C of the PV and TE module temperature difference.

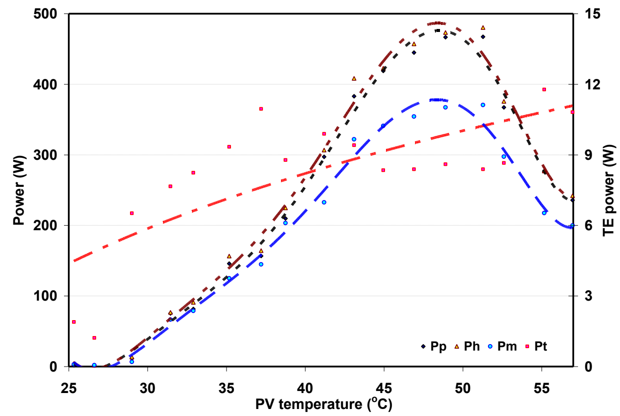

(a)

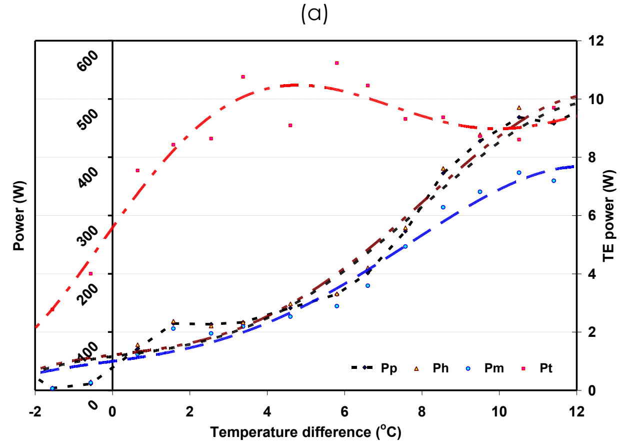

(b)

Figure 13 Typical powers versus (a) PV temperature and (b) temperature difference

Meanwhile, the thermoelectric power (Pt) increased considerably as the temperature difference rose, and it was further saturated at an increasing rate of 0.137 watts/°C. This power started to be saturated by 11.2 watts at 5.8°C of the temperature difference. The rising powers due to temperature differences are implied in [4, 11, 37].

Figure 14(a) shows the daily typical generated powers on the PV modules (Pp), TE modules (Pt), hybrid point (Ph), MPPT output (Pm), and inverter output (Pi). The three highest typical powers were the hybrid (Ph), PV (Pp), and MPPT output (Pm) powers. These typical powers had the most significant values on the fourth day at 383.6 watts, 372.7 watts, and 308.8 watts. These values were followed by those on the eighth day, as 315.8 watts, 310.2 watts, and 255.3

watts, and lastly followed by those on the second day, as 309.6 watts, 305.1 watts, and 255.3 watts, respectively. At the same time, the three highest typical TE powers were 11.56 watts, 11.23 watts, and 11.23 watts on the first, seventh, and eleventh days, respectively. These yielded powers are implied in [38, 55], which experienced daily variations.

Figure 14(b) shows the daily generated energy on the PV modules (Ep), TE modules (Et), hybrid point (Eh), MPPT output (Em), and inverter output (Ei). The three highest yielded hybrid energies were 3,260 Wh, 3,198 Wh, and 3,168 Wh, whereas the PV energies were 3,117 Wh, 3,067 Wh, and 3,096 Wh, on the eighth, second, and fifth day, respectively. The highest TE-generated energies were 109.40 Wh, 106.10 Wh, and 105.00 Wh on the first, eleventh, and seventh days, respectively. These yielded energies are implied in [38, 55], which experienced daily variations.

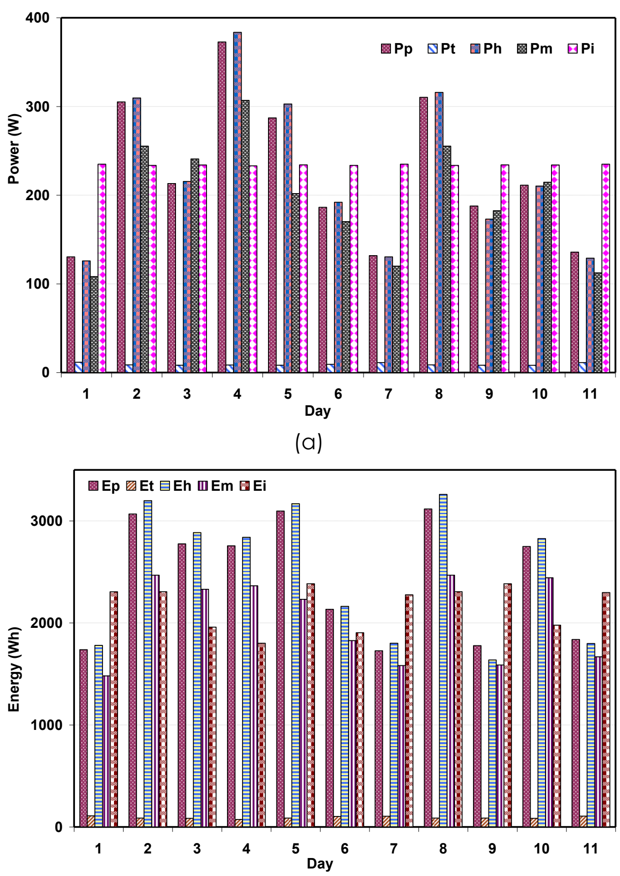

(a)

(b)

Figure 14 Daily typical generated (a) powers and (b) energies

Figure 15(a) shows the typical power-generated ratios in the hybrid to PV modules (Pp), TE modules (Pt), hybrid point (Ph), and MPPT output (Pm). Ef1, Ef2, Ef3, Ef4, Ef5, and Ef6 notations are ratios between Ph and summations of Pp and Pt, Pp and Ph, Pt, and Pp, Pt, and Ph, Pm, and Pp, and between Pm and Ph, respectively. Ef1 occupied the highest typical ratio of 99.40%. It was followed by Ef2, Ef5, Ef6, Ef3 and Ef4 which were 96.29%, 81.46%, 78.04%, 3.77% and 3.63%, respectively.

Figure 15(b) shows the typical energy-generated ratios in the hybrid to PV modules (Ep), TE modules (Et), hybrid point (Eh), and MPPT output (Em). Efe1, Efe2, Efe3, Efe4, Efe5, and Efe6 notations are ratios between Eh and summations of Ep and Et, Ep and Eh, Et and Ep, Et and Eh, Em and Ep, and between Em and Eh, respectively. The most significant ratio was Efe1 of 99.52%, followed by Efe2 of 97.27%. While the remaining ratios were 85.63%, 83.29%, 3.06%, and 2.98% for Efe5, Efe6, Efe3, and Efe4, respectively.

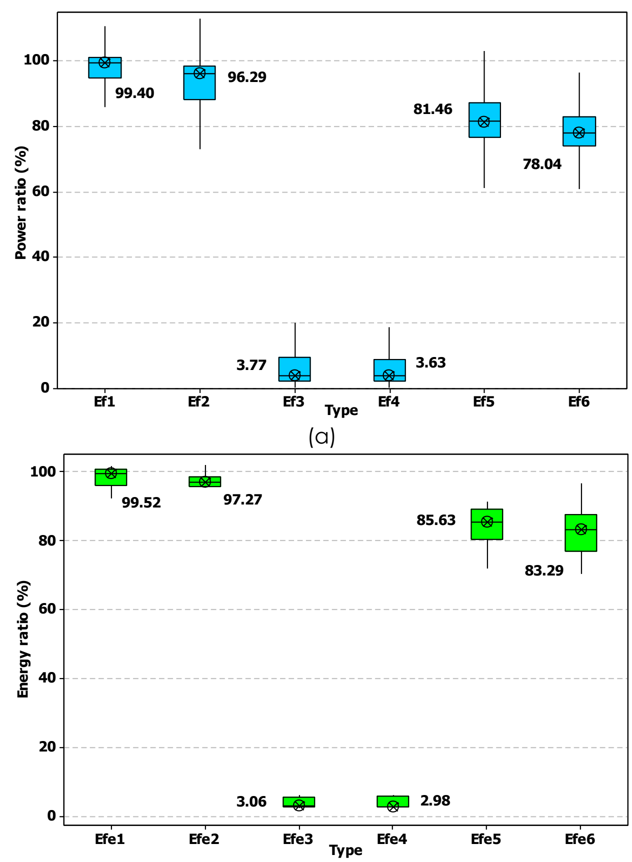

(a)

(b)

Figure 15 Typical (a) power and (b) energy ratios

4.0 CONCLUSION

The development of PVTE power hybrid generation and parameter internet-based recording system was successfully implemented. The temperatures, illuminance, UV radiation, humidity, air pollution, PV power, and TE power fluctuated daily. At the same time, the rainfall was an infrequent occurrence. Nevertheless, the rare rain was in the early morning and late afternoon, between 15:00 and 16:00.

The PV temperatures highly influenced the PV yielded power, with correlation coefficients between 0.810 and 0.829. While the TE temperatures moderately influenced the TE yielded power, with the correlation coefficients ranging from 0.357 to 0.406. Thus, the temperature influenced the PV modules more than the TE modules. Nevertheless, the increasing powers were limited by the temperatures.

The UV radiation and illuminance influenced the increase in the PV yielded power in the high correlation category, with 0.863 and 0.857 correlation coefficients, respectively. Meanwhile, the air temperature moderately influenced the enhancement of PV power, with a correlation coefficient of 0.428. Furthermore, the three environmental parameters; illuminance, UV radiation, and air temperature, were low enough to raise the TE-generated power. On the other hand, the humidity, air pollution, and rainfall factors were in moderate, low, and slight categories to decrease the PV yielded power, with -0.418, -0.294, and -0.084 correlation coefficients, respectively. The last three environmental parameters decreased the TE-produced power in low, slight, and slight categories, with -0.248, -0.125, and -0.006 correlation coefficients, respectively. Therefore, as much as possible, installing PVTE hybrid power generation should be avoided in areas with high humidity, air pollution, and rainfall.

The increasing PVTE produced powers due to the temperatures tended to reach maximum values and then further decrease. While the growing illuminance, UV radiation, and temperature differences enhanced the PVTE yielded powers and further saturated them. Therefore, a PVTE installation should be installed in areas with surrounding air temperature between 31.45 °C and 38.24 °C as much as possible.

The PV, TE, hybrid point, and MPPT output powers and energies were varied on various days, depending on the environmental conditions. At the same time, the inverter output power was reasonably stable. Nevertheless, at the last time of days, the inverter output power experienced a slight drop, probably caused by the slightly dropping battery energy.

The first and second highest power and energy ratios were occupied by the hybrid point and summation of PV and TE powers, as well as between PV and hybrid point powers. Both were above 95.0%. The third and fourth highest power and energy ratios were employed by those between MPPT output and PV and between the MPPT output and the hybrid point, as in a 75.0% and 90.0% range. Finally, the last ones were under 5.0%, namely the power and energy ratios between TE and PV and between TE and hybrid points.

Acknowledgement

This research is fully supported by the DIKTI grant, 325/B.005/LPPM/ITENAS/VI/2024. The authors fully acknowledged the Directorate General of Higher Education, Research, and Technology, the Ministry of Education, Culture, Research, and Technology, and the Republic of Indonesia for the approved funding, which makes this important research viable and effective.

Conflicts of Interest

The authors declare that there is no conflict of interest regarding the publication of this paper.

References

[1] Murphy, D. J., K. Goggin, and R. R. M. Paterson. 2021. Oil Palm in the 2020s and Beyond: Challenges and Solutions. *CABI Agriculture and Bioscience*. 2(1): 39. https://doi.org/10.1186/s43170-021-00058-3.

[2] Awoh, E. T., J. Kiplagat, S. K. Kimutai, and A. C. Mecha. 2023. Current Trends in Palm Oil Waste Management: A Comparative Review of Cameroon and Malaysia. *Heliyon*. 9(11). https://doi.org/10.1016/j.heliyon.2023.e21410.

[3] Obada, D. O., M. O. Kekung, T. Levonyan, and G. W. Norval. 2023. Palm Oil Mill Derived Empty Palm Fruit Bunches as a Feedstock for Renewable Energy Applications in Nigeria: A Review. *Bioresource Technology Reports*. 24: 101666. https://doi.org/10.1016/j.biteb.2023.101666.

[4] Li, J., D. Guan, S. Xia, Y. Fan, K. Zhao, Z. Zhao, *et al.* 2024. Recent Advances, Challenges, and Opportunities in Lignin Valorization for Value-Added Chemicals, Biofuels, and Polymeric Materials. *Energy Conversion and Management*. 322: 119123. https://doi.org/10.1016/j.enconman.2024.119123.

[5] Rashid, T., S. Ali Ammar Taqvi, F. Sher, S. Rubab, M. Thanabalan, M. Bilal, *et al.* 2021. Enhanced Lignin Extraction and Optimisation from Oil Palm Biomass Using Neural Network Modelling. *Fuel*. 293: 120485. https://doi.org/10.1016/j.fuel.2021.120485.

[6] Saberi Riseh, R., F. Fathi, A. Lagzian, M. Vatankhah, and J. F. Kennedy. 2024. Modifying Lignin: A Promising Strategy for Plant Disease Control. *International Journal of Biological Macromolecules*. 271: 132696. https://doi.org/10.1016/j.ijbiomac.2024.132696.

[7] Choi, S. J., Z. Lee, S. Kim, E. Jeong, and J. S. Shim. 2023. Modulation of Lignin Biosynthesis for Drought Tolerance in Plants. *Frontiers in Plant Science*. 14. https://doi.org/10.3389/fpls.2023.1116426.

[8] Beig, B., M. Riaz, S. Raza Naqvi, M. Hassan, Z. Zheng, K. Karimi, *et al.* 2021. Current Challenges and Innovative Developments in Pretreatment of Lignocellulosic Residues for Biofuel Production: A Review. *Fuel*. 287: 119670. https://doi.org/10.1016/j.fuel.2020.119670.

[9] Zhang, J., Y. Wang, X. Du, and Y. Qu. 2020. Selective Removal of Lignin to Enhance the Process of Preparing Fermentable Sugars and Platform Chemicals from Lignocellulosic Biomass. *Bioresource Technology*. 303: 122846. https://doi.org/10.1016/j.biortech.2020.122846.

[10] Wu, Z., N. Wang, H. Hisano, Y. Cao, F. Wu, W. Liu, *et al.* 2019. Simultaneous Regulation of F5H in COMT-RNAi Transgenic Switchgrass Alters Effects of Suppression on Syringyl Lignin Biosynthesis. *Plant Biotechnology Journal*. 17(4): 836–45. https://doi.org/10.1111/pbi.13019.

[11] Ahmad, K., and R. Ming. 2024. Harnessing Genetic Tools for Sustainable Bioenergy: A Review of Sugarcane Biotechnology in Biofuel Production. *Agriculture*. 14(8): 1312. https://doi.org/10.3390/agriculture14081312.

[12] Yusuf, C. Y. L., N. S. Nabilah, N. A. A. M. Taufik, I. A. Seman, and M. P. Abdullah. 2022. Genome-Wide Analysis of the CAD Gene Family Reveals Two Bona Fide CAD Genes in Oil Palm. *3 Biotech*. 12(7): 149. https://doi.org/10.1007/s13205-022-03208-0.

[13] Farhan, A. M., M. S. Hilman, M.-O. Abdullah, M. Y. Abdul Masani, N. A. Shaharuddin, and C. Y. L. Yusuf. 2024. Genetic Engineering of Lignin Biosynthesis for Enhanced Plant Traits: Applications in Bioenergy, Agriculture and Industry—A Review. *GADING Journal of Science and Technology*. 7(2): 73–84. https://myjms.mohe.gov.my/index.php/gjst/article/view/27379.

[14] Li, X., W. Chen, Y. Zhao, Y. Xiang, H. Jiang, S. Zhu, *et al.* 2013. Downregulation of Caffeoyl-CoA O-Methyltransferase (CCoAOMT) by RNA Interference Leads to Reduced Lignin Production in Maize Straw. *Genetics and Molecular Biology*. 36(4): 540–46. https://doi.org/10.1590/S1415-47572013005000039.

[15] Huang, S., X. Kang, R. Fu, L. Zheng, P. Li, F. Tang, *et al*. 2024. Simultaneous Down-Regulation of Dominant Cinnamoyl CoA Reductase and Cinnamyl Alcohol Dehydrogenase Dramatically Altered Lignin Content in Mulberry. *Plants.* 13(24). https://doi.org/10.3390/plants13243512.

[16] Song, Z., J. Liu, and H. Yang. 2021. Air Pollution and Soiling Implications for Solar Photovoltaic Power Generation: A Comprehensive Review. *Applied Energy*. 298: 117247. https://doi.org/10.1016/j.apenergy.2021.117247.

[17] El Kassar, R., A. Al Takash, J. Faraj, M. Khaled, and H. S. Ramadan. 2025. Phase Change Materials for Enhanced Photovoltaic Panels Performance: A Comprehensive Review and Critical Analysis. *Energy and Built Environment*. 6: 655–675. https://doi.org/10.1016/j.enbenv.2024.02.004.

[18] Yao, W., X. Kong, A. Xu, P. Xu, Y. Wang, and W. Gao. 2023. New Models for the Influence of Rainwater on the Performance of Photovoltaic Modules Under Different Rainfall Conditions. *Renewable and Sustainable Energy Reviews.* 173: 113119. https://doi.org/10.1016/j.rser.2022.113119.

[19] Simsek, E., M. J. Williams, and L. Pilon. 2021. Effect of Dew and Rain on Photovoltaic Solar Cell Performances. *Solar Energy Materials and Solar Cells.* 222: 110908. https://doi.org/10.1016/j.solmat.2020.110908.

[20] Stankov, B., A. Terziev, M. Vassilev, and M. Ivanov. 2024. Influence of Wind and Rainfall on the Performance of a Photovoltaic Module in a Dusty Environment. *Energies.* 17: 3394. https://doi.org/10.3390/en17143394.

[21] Nagaraja, M. R., W. K. Biswas, and C. P. Selvan. 2025. Advancements and Challenges in Solar Photovoltaic Technologies: Enhancing Technical Performance for Sustainable Clean Energy – A Review. *Solar Energy Advances.* 5: 100084. https://doi.org/10.1016/j.seja.2024.100084.

[22] Waluyo, D., A. R. Darlis, F. Hadiatna, and A. Abimanyu. 2024. Influences of Environmental Factors of a Hybrid Photovoltaic and Thermoelectric Generation System. *ELKOMIKA*. 12(4): 1038–1050. https://doi.org/10.26760/elkomika.v12i4.1038.

[23] Rajasekar, S. 2024. *Numerical Methods: Classical and Advanced Topics*. 1st ed. Boca Raton: CRC Press. https://doi.org/10.1201/9781032649931-10.

[24] Tredoux, C., and K. Durrheim. 2019. *Numbers, Hypotheses & Conclusions: A Course in Statistics for the Social Sciences*. 3rd ed. Cape Town: Juta and Company (Pty) Ltd.

[25] Härdle, W. K., L. Simar, and M. R. Fengler. 2024. *Applied Multivariate Statistical Analysis*. 6th ed. Cham: Springer Nature. https://doi.org/10.1007/978-3-031-63833-6.

[26] Kong, X., J. Luo, and X. Feng. 2024. *Process Monitoring and Fault Diagnosis Based on Multivariable Statistical Analysis*. Beijing: Science Press. https://doi.org/10.1007/978-981-99-8775-7.

[27] Maiti, J. 2023. *Multivariate Statistical Modeling in Engineering and Management*. Boca Raton: CRC Press. https://doi.org/10.1201/9781003303060.

[28] Bruce, P., A. Bruce, and P. Gedeck. 2020. *Practical Statistics for Data Scientists*. 2nd ed. Sebastopol: O'Reilly Media.

[29] Geng, X., M. Qi, J. Liu, C. He, and Y. Li. 2021. Application of Principal Component Analysis on Water Flooding Effect Evaluation in Natural Edge Bottom Water Reservoir. *Journal of Petroleum Exploration and Production Technology.* 11(1): 439–449. https://doi.org/10.1007/s13202-020-01055-4.

[30] Martínez-García, F. M., A. Molina-García, M. Alarcón, and F. C. G. de León. 2026. Distillation Anomaly and Fault Detection Based on Unsupervised Dimensionality Principal Component Analysis Method. *Measurement.* 258: 119261. https://doi.org/10.1016/j.measurement.2025.119261.

[31] Holubova, H. 2023. A Comparative Analysis of the Principal Component Method and Parallel Analysis in Working with Official Statistical Data. *Statistics in Transition New Series.* 24(1): 199–212. https://doi.org/10.59170/stattrans-2023-011.

[32] Hasanzadeh, H., S. A. Mohammadi, M. B. Shafii, and M. Daneshvar. 2025. Designing and Constructing a Solar Thermal Water Desalination System: Evaluating the Role of Thermoelectric in Enhancing Evaporation and Condensation Process. *Next Energy*. 9: 100388. https://doi.org/10.1016/j.nxener.2025.100388.

[33] Congxiang, T., G. Zhang, and Y. Yong. 2025. Hybrid Photovoltaic and Thermoelectric Generator Systems with Thermal Wheel Ventilation: A Sustainable Approach to Residential Heating and Cooling. *Engineering Science and Technology, an International Journal*. 62: 101968. https://doi.org/10.1016/j.jestch.2025.101968.

[34] Hsieh, C.-C., K. Debnath, J. Barman, C.-Y. Huang, C.-H. Yang, N.-Y. Chu, C.-W. Chiu, and C.-F. J. Kuo. 2025. Performance and Economic Evaluation of Monofacial and Bifacial Floating Photovoltaic Systems in Taiwan's Coastal Marine Climate. *Case Studies in Thermal Engineering*. 75: 107130. https://doi.org/10.1016/j.csite.2025.107130.

[35] Gupta, R. K., and D. K. Molzahn. 2025. Improving Fairness in Photovoltaic Curtailment via Feedback-Driven Daily Topology Reconfiguration in Power Distribution Networks. *Applied Energy*. 400: 126543. https://doi.org/10.1016/j.apenergy.2025.126543.

[36] Žižak, T., S. Medved, and C. Arkar. 2025. Effect of Solar Photovoltaics on Green Roof Energy Balance and Evapotranspiration. *Sustainable Cities and Society*. 121: 106206. https://doi.org/10.1016/j.scs.2025.106206.

[37] Rajpar, A. H., M. B. A. Bashir, E. Y. Salih, E. M. Ahmed, and A. M. Soliman. 2024. Efficiency Enhancement of Photovoltaic-Thermoelectric Generator Hybrid Module by Heat Dissipating Technique. *Results in Engineering.* 24: 102907. https://doi.org/10.1016/j.rineng.2024.102907.

[38] Zhu, Y., D. W. Newbrook, P. Dai, J. Liu, J. Li, C. Wang, H. M. Chong, C. H. K. de Groot, and R. Huang. 2024. Artificial Neural Network Enabled Photovoltaic-Thermoelectric Generator Modelling and Analysis. *Case Studies in Thermal Engineering.* 61: 105053. https://doi.org/10.1016/j.csite.2024.105053.

[39] Shen, Z.-H., H. Ni, C. Ding, G.-R. Sui, H.-Z. Jia, X.-M. Gao, and N. Wang. 2021. Improving the Energy-Conversion Efficiency of a PV–TE System with an Intelligent Power-Track Switching Technique and Efficient Thermal-Management Scheme. *IEEE Transactions on Components, Packaging and Manufacturing Technology*. 11(6): 963–973. https://doi.org/10.1109/TCPMT.2021.3074529.

[40] Moore, J., and G. Iglesias. 2025. Hybridisation of Offshore Wind Farms with Floating Photovoltaics: Power Smoothing and Output-Demand Divergence Reduction. *Energy Conversion and Management.* 345: 120413. https://doi.org/10.1016/j.enconman.2025.120413.

[41] Teixeira, H., M. G. Gomes, A. M. Rodrigues, and D. Aelenei. 2024. Solar Responsive Building Glazing: Experimental Analysis of the Impact of Photochromic Glazing on Indoor Thermal and Luminous Conditions. *Journal of Building Engineering.* 92: 109812. https://doi.org/10.1016/j.jobe.2024.109812.

[42] Gundogdu, H., M. Terkes, A. Demirci, and U. Cali. 2024. Assessing Energy Savings and Visual Comfort with PDLC-Based Smart Window in an Istanbul Office Building. *Energy Reports.* 12: 4252–4265. https://doi.org/10.1016/j.egyr.2024.10.009.

[43] Li, X., K. Li, Y. Sun, R. Wilson, J. Peng, K. Shanks, T. Mallick, and Y. Wu. 2024. Comprehensive Investigation of a Building Integrated Crossed Compound Parabolic Concentrator Photovoltaic Window System: Thermal, Optical and Electrical Performance. *Renewable Energy*. 223: 119791. https://doi.org/10.1016/j.renene.2023.119791.

[44] Khalil, S. A., U. A. Rahoma, A. H. Hassan, and R. M. Greeb. 2021. Assessment of UVB Solar Radiation in Four Different Selected Climate Locations in Saudi Arabia. *NRIAG Journal of Astronomy and Geophysics*. 10(1): 125–137. https://doi.org/10.1080/20909977.2021.1898142.

[45] García-Rodríguez, S., I. García, A. García-Rodríguez, M. Díez-Mediavilla, and C. Alonso-Tristán. 2022. Solar Ultraviolet Irradiance Characterization under All Sky Conditions in Burgos, Spain. *Applied Sciences*. 12: 10407. https://doi.org/10.3390/app122010407.

[46] Mohamed, M. S., M. M. A. Wahab, M. El-Metwally, and E. F. El-Nobi. 2023. Validation of UV-Index Retrieved from Three Satellites Against Ground-Based Measurements at Different Climates in Egypt. *The Egyptian Journal of Remote Sensing and Space Sciences*. 26: 361–367. https://doi.org/10.1016/j.ejrs.2023.04.006.

[47] Malmgren, R., S. Sofieva-Rios, K. Lakkala, E. Asmi, Y. Sun, M. Todt, P. Heikkilä, D. Bamford, M. Romantschuk, and N. Atanasova. 2024. Phi6 Virus Transmission in Arctic Outdoor Air and the Effects of Solar UV Radiation on Virus and Host Viability. *Environmental Advances*. 18: 100600. https://doi.org/10.1016/j.envadv.2024.100600.

[48] Wang, J., X.-S. Wang, Z. Zhang, D.-Y. Zhou, L. Qin, and X.-H. Huang. 2024. Enhancing the Quality of Semi-Dried Tilapia Fillets Using Ultraviolet Radiation to Simulate the Natural Solar Drying Process. *LWT – Food Science and Technology*. 213: 117099. https://doi.org/10.1016/j.lwt.2024.117099.

[49] Riyadi, T. W. B., M. Effendy, B. R. Utomo, and A. T. Wijayanta. 2023. Performance of a Photovoltaic-Thermoelectric Generator Panel in Combination with Various Solar Tracking Systems. *Applied Thermal Engineering*. 235: 121336. https://doi.org/10.1016/j.applthermaleng.2023.121336.

[50] Pero, C. D., N. Aste, and F. Leonforte. 2021. The Effect of Rain on Photovoltaic Systems. *Renewable Energy*. 179: 1803–1814. https://doi.org/10.1016/j.renene.2021.07.130.

[51] Shittu, S., G. Li, X. Zhao, J. Zhou, X. Ma, and Y. G. Akhlaghi. 2020. Experimental Study and Exergy Analysis of Photovoltaic-Thermoelectric with Flat Plate Micro-Channel Heat Pipe. *Energy Conversion and Management*. 207: 112515. https://doi.org/10.1016/j.enconman.2020.112515.

[52] Algarni, S., and K. Irshad. 2023. Performance Evaluation of a Hybrid Thermoelectric Generator and Flat Plate Solar Collector System in a Semi-Arid Climate. *Case Studies in Thermal Engineering*. 44: 102842. https://doi.org/10.1016/j.csite.2023.102842.

[53] Oni, A. M., A. S. M. Mohsin, M. M. Rahman, and M. B. H. Bhuian. 2024. A Comprehensive Evaluation of Solar Cell Technologies, Associated Loss Mechanisms, and Efficiency Enhancement Strategies for Photovoltaic Cells. *Energy Reports.* 11: 3345–3366. https://doi.org/10.1016/j.egyr.2024.03.007.

[54] Lorenzi, B., P. Mariani, A. Reale, A. D. Carlo, G. Chen, and D. Narducci. 2021. Practical Development of Efficient Thermoelectric–Photovoltaic Hybrid Systems Based on Wide-Gap Solar Cells. *Applied Energy*. 300: 117343. https://doi.org/10.1016/j.apenergy.2021.117343.

[55] Yang, S., E. Yin, Q. Li, and Y. Long. 2024. Experimental Optimization of a Spectrum-Splitting Photovoltaic-Thermoelectric Hybrid System. *Applied Thermal Engineering*. 248(Part A): 123177. https://doi.org/10.1016/j.applthermaleng.2024.123177.